

Mass profiles and anisotropies of early-type galaxies

John Magorrian and David Ballantyne

*CITA, University of Toronto, 60 St George Street, Toronto, Ontario, Canada M5S 3H8, and
Institute of Astronomy, Madingley Road, Cambridge CB3 0HA*

ABSTRACT

We discuss the problem of using stellar kinematics of early-type galaxies to constrain the galaxies’ orbital anisotropies and radial mass profiles. We demonstrate that compressing a galaxy’s light distribution along the line of sight produces approximately the same signature in the line-of-sight velocity profiles as radial anisotropy. In particular, fitting spherically symmetric dynamical models to apparently round, isotropic face-on flattened galaxies leads to a spurious bias towards radial orbits in the models, especially if the galaxy has a weak face-on stellar disk. Such face-on stellar disks could plausibly be the cause of the radial anisotropy found in spherical models of intermediate luminosity ellipticals such as NGC 2434, NGC 3379 and NGC 6703.

In the light of this result, we use simple dynamical models to constrain the outer mass profiles of a sample of 18 round, early-type galaxies. The galaxies follow a Tully–Fisher relation parallel to that for spiral galaxies, but fainter by at least 0.8 mag (*I*-band) for a given mass. The most luminous galaxies show clear evidence for the presence of a massive dark halo, but the case for dark haloes in fainter galaxies is more ambiguous. We discuss the observations that would be required to resolve this ambiguity.

Key words: celestial mechanics – stellar dynamics – galaxies: kinematics and dynamics – galaxies: halos

1 INTRODUCTION

While it has long been known that spiral galaxies are embedded in halos of some kind of dark component, the evidence that ellipticals have dark halos is much more patchy. Analyses of the temperature profiles (e.g., Brighenti & Mathews 1997), the mean temperature (Loewenstein & White 1999) and the shapes (Buote & Canizares 1997) of the hot, X-ray emitting gas in bright ellipticals all demonstrate that these large galaxies have dark halos extending to many effective radii. Similarly, results from gravitational lensing studies (e.g., Kochanek 1996) show that the mass-to-light ratios of at least some large ellipticals must rise beyond an effective radius or so. It was unclear whether faint, compact ellipticals also had dark halos until the recent work of Rix et al. (1997) and Gerhard et al. (1998). These authors applied sophisticated spherical dynamical models to deep measurements of the line-of-sight velocity profiles (VPs) of the round galaxies NGC 2434 and NGC 6703. They found that the mass-to-light ratio in each rises outwards beyond about an effective radius. But despite this recent progress, our understanding of the properties of dark haloes of ellipticals remains poor.

The main difficulty in determining the mass distributions (or, equivalently, the potentials) of most ellipticals is the absence of dynamical tracers other than stars, planetary nebulae (PNe) and globular clusters. Since these tracers are collisionless, one cannot determine the galaxy’s potential without simultaneously constraining the distribution of orbits of the tracer population (the orbit distribution

function, or DF) within the galaxy. There are two general approaches to this problem. One is to consider a range of parametrized trial galaxy potentials and, for each trial potential, to search for the DF that best matches the observed VPs. Potentials for which no satisfactory fit can be found can be ruled out. This is the approach used by Merritt & Saha (1993), Merritt (1993), Rix et al. (1997) and Gerhard et al. (1998). An alternative approach is to consider a range of simple parametrized forms for the DF and to search for the mass distributions consistent with the assumed DFs and the available observations. This has been used by Merritt & Tremblay (1993), Gebhardt & Fischer (1995) and Merritt (1996), but only considering one form for the DF (isotropy) and without making full use of the information contained in the observed VPs. We follow this second approach in the present paper, but using a wider range of parametrized DFs and making fuller use of observed VPs.

The paper is organized as follows. In common with most other work in this area, our models assume spherical symmetry for convenience. So, we begin in §2 by identifying the biases that this assumption introduces. In §3 we consider the simple problem of determining, for a spherical galaxy, the range of mass-to-light ratio profiles consistent with an observed velocity dispersion profile and some assumed form for the anisotropy of the velocity dispersion tensor. Section 4 then shows how this method can naturally be extended to use VP shape information, including information from discrete tracers of the VPs, such as PNe. Applications to real galaxies follow in §5, before we sum up in §6.

2 THE DEGENERACY BETWEEN MASS, ANISOTROPY AND FLATTENING

Throughout this paper we will assume that our round galaxies are close to spherical. Before plunging into the details of the modelling procedure, let us first pause to consider the consequences of this assumption. It is instructive to take a real galaxy as an example. We use NGC 2434, an E0 studied in detail by Rix et al. (1997).

The points on Figure 1(a) plot the observed stellar kinematics of this galaxy. In addition to the usual velocity dispersion σ , there is a Gauss–Hermite parameter h_4 that measures the deviation of the observed VP from the underlying best-fit Gaussian (van der Marel & Franx 1993). VPs more boxy than Gaussian have $h_4 < 0$, whereas those more triangular have $h_4 > 0$. The dashed curves plot the kinematics of a spherical model galaxy with the same projected light distribution as NGC 2434, an isotropic velocity distribution, and an isothermal potential with $v_c = 300 \text{ km s}^{-1}$. The model reproduces the observed velocity dispersion quite well, but not the shapes of the VPs – its VPs are not centrally peaked enough. This can be rectified by increasing the fraction of stars on radial orbits in the model, while keeping the light distribution and potential fixed. Indeed, Rix et al. (1997) have used sophisticated modelling machinery based on Schwarzschild’s (1979) method to construct a strongly radially anisotropic spherical model that provides an excellent fit to the observed kinematics of this galaxy.

It turns out, however, that there is no need to invoke radial anisotropy to explain these kinematics. Let us start with the spherical isotropic model again, but, instead of increasing the fraction of stars on radial orbits, let us keep the velocity distribution isotropic while flattening the model along the line of sight. Flattening the model like this increases the fraction of stars orbiting in the plane of the sky (i.e., orbits with high L_z) and decreases the model’s projected velocity dispersion. This was first noted by Bender, Saglia & Gerhard (1994), who invoked almost face-on circular orbits in a similar way to explain the minor-axis VPs of NGC 4660. The extra orbits in the plane of the sky affect the VP shapes in the same way as a bias towards radial orbits in a spherical galaxy.

To give a more concrete example, we have increased the mass of our spherical isotropic model of NGC 2434 from $v_c = 300 \text{ km s}^{-1}$ to 400 km s^{-1} , and squeezed its light distribution by first making it oblate with axis ratio $q = 0.6$ and then adjusting its $\cos 4\theta$ Fourier coefficients until its edge-on projected surface brightness distribution has the form shown in Figure 1(b). The a_4 coefficient on this plot measures the lowest-order symmetric deviation of each isophote from the underlying best-fit ellipse. The model is quite disk-like ($a_4 > 0$), with a peak a_4/a of 3.7% when viewed edge-on, or 1.9% when averaged over all viewing angles.

We calculate the kinematics of the model using the method described in Magorrian & Binney (1994). The results are plotted as the heavy curves on Figure 1(a). This flattened, isotropic model provides just as good a fit to the observations as the radially anisotropic, spherical models of Rix et al. (1997). While the diskiness of our model affects the shape of its VPs when seen face-on, even when seen edge on the disk does not have a strong effect on the model’s (v_0/σ), the characteristic ratio of the mean-streaming velocity to the

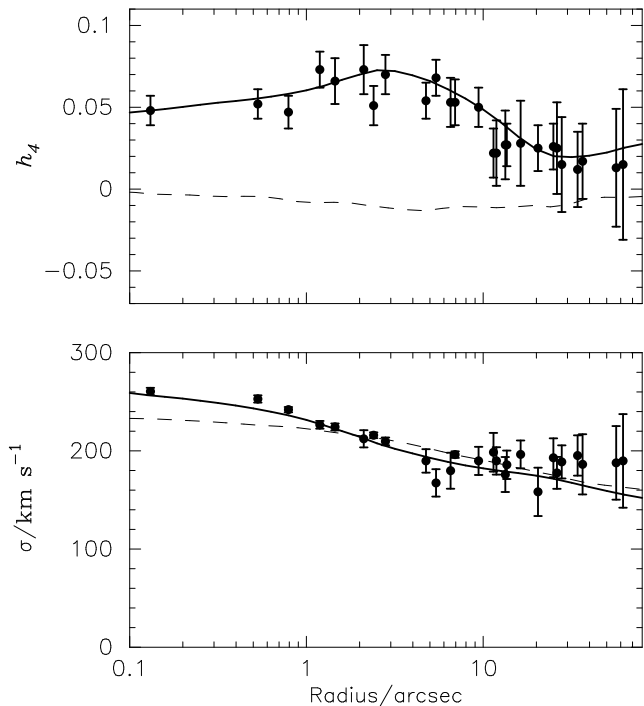


Figure 1(a). Kinematics of the E0 galaxy NGC 2434. The points on plot the observed velocity dispersion σ and Gauss–Hermite VP shape parameter h_4 versus radius. The broken curves plot the corresponding quantities for spherical isotropic galaxy models. The heavy solid curves show the kinematics of an flattened isotropic model of the galaxy, viewed face-on. Figure 1(b) shows the edge-on surface brightness distribution of this model.

velocity dispersion (Binney 1978; Davies et al. 1983). This remains very close to the predictions for an oblate isotropic rotator.

Of course, these results do not mean that NGC 2434 *must* be isotropic with a weak face-on stellar disk, but they do show that making unwarranted assumptions about a galaxy’s intrinsic shape will lead to biases in the orbit distribution that one finds. Throughout the rest of this paper we will model our round galaxies under the assumption of spherical symmetry. In Appendix A we quantify the degeneracy between mass, anisotropy and shape, showing how the results from our spherical models may be corrected for any supposed degree of (constant) flattening.

3 CONSTRAINING THE MASS PROFILE USING VELOCITY DISPERSION MEASUREMENTS

We are given measurements of a galaxy’s projected velocity dispersion σ_i with corresponding errors (assumed Gaussian) $\Delta\sigma_i$ at points R_i , with $i = 1 \dots N$. The luminosity density of the galaxy is $j(r)$. We seek the range of smooth mass-to-light ratio profiles $\Upsilon(r)$ consistent with these observations and some assumed form for $\beta(r)$, the anisotropy of the galaxy’s velocity dispersion tensor, where

$$\beta(r) \equiv 1 - \frac{\sigma_\phi^2(r)}{\sigma_r^2(r)}, \quad (1)$$

and $\sigma_r(r)$ and $\sigma_\phi(r)$ are the velocity dispersions in the radial and azimuthal directions at radius r . Before explaining

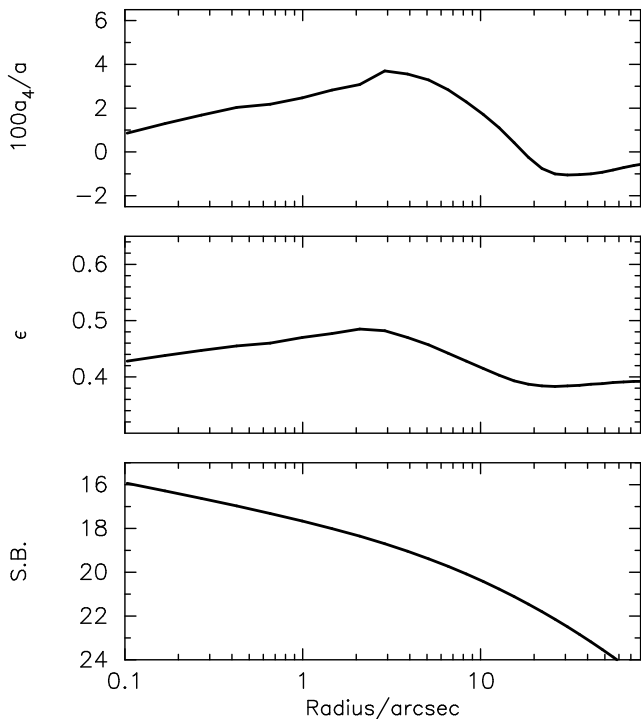


Figure 1(b). Edge-on surface brightness distribution of the flattened isotropic model in Fig. 1(a). The panels show the model’s isophotal shape parameters (surface brightness, ellipticity and lowest-order shape parameter a_4/a), using the convention of Bender & Möllenhoff (1987).

how we determine the range of $\Upsilon(r)$, we first describe the necessary simpler step in the method: how to calculate the predicted velocity dispersion profile $\hat{\sigma}(R)$ of a trial $\Upsilon(r)$.

3.1 From $\Upsilon(r)$ to $\hat{\sigma}(R)$

Given $\Upsilon(r)$, the mass interior to radius r is given by

$$M(r) = 4\pi \int_0^r \Upsilon(r') j(r') r'^2 dr'. \quad (2)$$

The Jeans equation (e.g., Binney & Tremaine 1987),

$$\frac{d(j\bar{v}_r^2)}{dr} + 2\beta \frac{j\bar{v}_r^2}{r} = -j \frac{GM}{r^2}, \quad (3)$$

can be integrated to give the intrinsic second-order moments in terms of $j(r)$, $M(r)$ and $\beta(r)$:

$$j\bar{v}_r^2(r) = \int_r^\infty dr' \nu(r') \frac{GM(r')}{r'^2} \exp \left[\int_r^{r'} \frac{2\beta(r'')}{r''} dr'' \right], \quad (4)$$

and, by definition,

$$\bar{v}_\phi^2 = \bar{v}_\theta^2 = (1 - \beta)\bar{v}_r^2. \quad (5)$$

Projecting along lines of sight, the zeroth and second-order moments at projected radius R are

$$\begin{aligned} I(R) &= 2 \int_R^\infty \frac{j(r)r dr}{\sqrt{r^2 - R^2}} \\ I\bar{v}_p^2(R) &= 2 \int_R^\infty \frac{j\bar{v}_r^2(r)r dr}{\sqrt{r^2 - R^2}} \left(1 - \beta(r) \frac{R^2}{r^2} \right). \end{aligned} \quad (6)$$

To include the effects of seeing, we assume that the PSF of the kinematic observations is a Gaussian with dispersion $\sigma_* = \text{FWHM}/2.305$,

$$\text{PSF}(\Delta x) = \frac{1}{2\pi\sigma_*^2} \exp \left[-\frac{1}{2} \left(\frac{\Delta x}{\sigma_*} \right)^2 \right]. \quad (7)$$

The convolution of any projected distribution $\mu_0(R)$ (e.g., $I(R)$ or $I\bar{v}_p^2(R)$) with this PSF is

$$\begin{aligned} \mu(R) &= \frac{1}{\sigma_*^2} \exp \left(-\frac{R^2}{2\sigma_*^2} \right) \times \\ &\int_0^\infty R' \exp \left(-\frac{R'^2}{2\sigma_*^2} \right) I_0 \left(\frac{RR'}{\sigma_*^2} \right) \mu_0(R') dR', \end{aligned} \quad (8)$$

where $I_0(x)$ is the zeroth-order modified Bessel function. Dividing the seeing-convolved second-order moment by the zeroth order one and taking the square root yields the model’s predicted $\hat{\sigma}(R)$, and, in particular, its predictions $\hat{\sigma}_i$ at the observed points R_i .

In the numerical implementation of the calculations above we store the logarithms of $j(r)$, $M(r)$, etc. on grids spaced logarithmically in radius from the radius of the innermost observed isophote to a few times the radius of the outermost one, typically with about 30 grid points. Values of $j(r)$, $M(r)$, etc. at intermediate points are obtained by linear interpolation on these log-log grids and exponentiating. Since the positions of the radial grid points, as well as $j(r)$ and $\beta(r)$, are independent of $\Upsilon(r)$, many of the coefficients involved in the numerical calculation of the integrals (2), (4), (6) and (8) need only be evaluated once, leading to a considerable decrease in the time needed to calculate the $\hat{\sigma}_i$ from a trial $\Upsilon(r)$.

3.2 Determining the range of acceptable $\Upsilon(r)$

By Bayes’ theorem, the probability of any model $\Upsilon(r)$ given the available velocity dispersion data D and our assumed β satisfies

$$\mathcal{P} \equiv p(\Upsilon|D, \beta) \propto p(D|\Upsilon, \beta) p(\Upsilon). \quad (9)$$

Since we assume that the observational errors are Gaussian, the likelihood $p(D|\Upsilon, \beta)$ is given by

$$p(D|\Upsilon, \beta) = \exp \left(-\frac{1}{2} \chi^2 \right), \quad (10)$$

where

$$\chi^2[\Upsilon, \beta] = \sum_{i=1}^N \left(\frac{\hat{\sigma}_i - \sigma_i}{\Delta\sigma_i} \right)^2. \quad (11)$$

The prior $p(\Upsilon)$ encodes our prejudices about what constitutes a reasonable $\Upsilon(r)$. Our only expectation is that it be smooth, and we take

$$\ln p(\Upsilon) = -\lambda \int \left(\frac{d^2 \ln \Upsilon}{d(\ln r)^2} \right)^2 d \ln r \cdot \int d \ln r, \quad (12)$$

which uses the mean-square change in the slope of $\ln \Upsilon$ versus $\ln r$ as a measure of smoothness. For a reasonable $\Upsilon(r)$ the change in the mean-square slope would be less than about 100. We set $\lambda = 1/100$ so that an increase in the mean-square slope by 100 has the same effect on $p(\Upsilon|D, \beta)$ as an increase in χ^2 of one.

To obtain the range of $\Upsilon(r)$ that maximize \mathcal{P} , we first fit an initial guess of the form

$$\Upsilon(r) = \Upsilon_0 \left(\frac{r}{r_0}\right)^a \left(1 + \frac{r}{r_0}\right)^b, \quad (13)$$

using the downhill simplex method (Press et al. 1992) to find the parameters (Υ_0, r_0, a, b) that minimize χ^2 in equation (11). Then the Metropolis algorithm (Metropolis et al. 1953) is used to explore the range of $\Upsilon(r)$ consistent with the data:

- (1) Calculate $\mathcal{P}[\Upsilon]$ for the initial guess.
- (2) Make a change $\delta\Upsilon$ to Υ . Calculate $\chi^2[\Upsilon + \delta\Upsilon]$, $p(\Upsilon + \delta\Upsilon)$ and thus $\mathcal{P}[\Upsilon + \delta\Upsilon]$.
- (3) if $\Delta\mathcal{P} \equiv \mathcal{P}[\Upsilon + \delta\Upsilon] - \mathcal{P}[\Upsilon] > 0$ accept the change $\delta\Upsilon$; otherwise accept it with probability $\exp(\Delta\mathcal{P})$.
- (4) Go back to step 2.

Each change $\delta\Upsilon$ in step (2) is made by choosing a single radial grid point i at random and adding $x\Delta_i$ to $\ln \Upsilon_i$, where x is a random number uniformly distributed in $(-1, 1)$ and the constant Δ_i sets the size of the maximum change in $\ln \Upsilon$ at the point i . For maximum efficiency the Δ_i should be chosen so that the change in each step of the Metropolis algorithm has roughly equal chances of being accepted or rejected. We ensure this is the case by initially choosing all $\Delta_i = 1$ and following the Metropolis algorithm from the initial fit (13) for enough iterations to ensure that each radial grid point is sampled many times. During this time, we increase Δ_i by a small factor (e.g., 1.5) if a change in the i^{th} grid point is accepted, and decrease it by the same factor if the change is rejected. We then restart the Metropolis algorithm from the initial fit (13) keeping the Δ_i fixed.

As the Metropolis algorithm progresses, the probability of any given configuration $\Upsilon(r)$ occurring tends towards the probability $p(\Upsilon|D, \beta) \equiv \mathcal{P}$. This makes it easy to obtain confidence intervals on $\Upsilon(r)$ and other model quantities. In addition, if we have two models, one with anisotropy $\beta_1(r)$, the other with $\beta_2(r)$, and no reason for favouring one over the other ($p(\beta_1) = p(\beta_2)$), then a simple application of Bayes' theorem yields their relative probability,

$$\frac{p(\beta_1|D)}{p(\beta_2|D)} = \frac{p(D|\beta_1)}{p(D|\beta_2)} = \frac{\int p(D|\Upsilon, \beta_1) p(\Upsilon) d\Upsilon}{\int p(D|\Upsilon, \beta_2) p(\Upsilon) d\Upsilon}, \quad (14)$$

which from equation (9) is just the ratio of the average values of \mathcal{P} in the Metropolis algorithm. Of course, equation (14) is not very useful in the present case, since for most choices of $\beta(r)$ there is usually some smooth $\Upsilon(r)$ that projects to a good fit to the observed σ_i . But given further information on the shapes of the VPs (Section 4), and if we somehow knew that the galaxy was close to spherical, we could use equation (14) to distinguish between models with different $\beta(r)$.

3.3 An application to M87

In principle, the mass profile can also be obtained by rearranging the Jeans equation (3) to get

$$M(r) = -\frac{rv_r^2}{G} \left(\frac{d \ln j}{d \ln r} + \frac{d \ln \overline{v_r^2}}{d \ln r} + 2\beta \right), \quad (15)$$

in which $\overline{v_r^2}$ follows from an inversion of equation (6). This approach was used by Sargent et al. (1978) to obtain the

mass distribution of M87 assuming that it is isotropic ($\beta = 0$). The method is very direct, but requires the fitting of a smooth, arbitrary $\sigma(R)$ profile to the observed σ_i , leading to complex biases in the results. Here we use Sargent et al.'s data and results to provide a simple test of our method.

We obtain our model luminosity density $j(r)$ from their photometry using the method described in Magorrian (1999). It is unclear exactly what seeing was in effect at the time of Sargent et al.'s observations, but we assume 2 arcsec FWHM. We then apply the algorithm above to their kinematical data for 10^5 iterations, the results of which are plotted on Fig. 2. The panels show the 95% confidence limits on the local mass-to-light ratio $\Upsilon(r)$, the ‘‘average’’ mass-to-light ratio $M(r)/L(r)$ enclosed within radius r , and the corresponding limits on the model's projected dispersion profile $\hat{\sigma}(r)$, together with the observed σ_i . The values of $M(r)/L(r)$ found by Sargent et al. are also plotted on Fig. 2 for comparison with ours. There is quite good agreement between our results and theirs, except within the innermost few arcsec of the galaxy centre. The reason for this is simple (e.g., Binney & Tremaine 1987): at large radii, the $j(r)$ profile is steep ($\sim r^{-3}$) while the v_r^2 profile is shallow ($\sim r^0$), so that the value of the bracketed expression in (15) used by Sargent et al. is dominated by the relatively well-determined slope of $j(r)$. At smaller radii, $j(r)$ becomes much shallower, v_r^2 steepens, and so $M(r)$ is affected more by the poorly determined slope of the latter.

While the agreement between the results from the two methods is gratifying, it is important to note the fundamental difference between them. In methods like Sargent et al.'s (e.g., Gebhardt & Fischer 1995), one is required to make assumptions about unobserved data, whereas in methods like ours (e.g., Merritt & Tremblay 1993; Merritt 1996) one uses only real, observed data, and confines any assumptions to the model itself. In the former case, there is no straightforward way to obtain confidence bounds on the model's mass density profiles, or indeed to impose the reasonable constraint that the mass density must be non-negative. On the other hand, our model's disregard for imaginary data is why the exact amount of mass enclosed within the innermost few arcsec is quite uncertain – due to the effects of seeing, the data are consistent with quite a gentle increase in mass-to-light ratio near the centre. Similarly, our model correctly reproduces the fact that there are no interesting constraints on $\Upsilon(r)$ beyond the radius of the outermost observed dispersion. Of course, the one big advantage of methods like Sargent et al.'s over ours is that they are relatively quick, and can be adequate if one is content with finding only a restricted range of the full set of plausible mass density profiles.

4 USING VELOCITY PROFILES TO CONSTRAIN BOTH THE MASS PROFILE AND THE ANISOTROPY

The method above can be extended to make use of the full observed VPs if, instead of assuming a form for $\beta(r)$, we make a stronger assumption about the form of the galaxy's distribution function (DF). By Jeans' theorem, the DF of a spherical galaxy is a function only of the stars' binding energies \mathcal{E} and angular momenta L per unit mass. We make

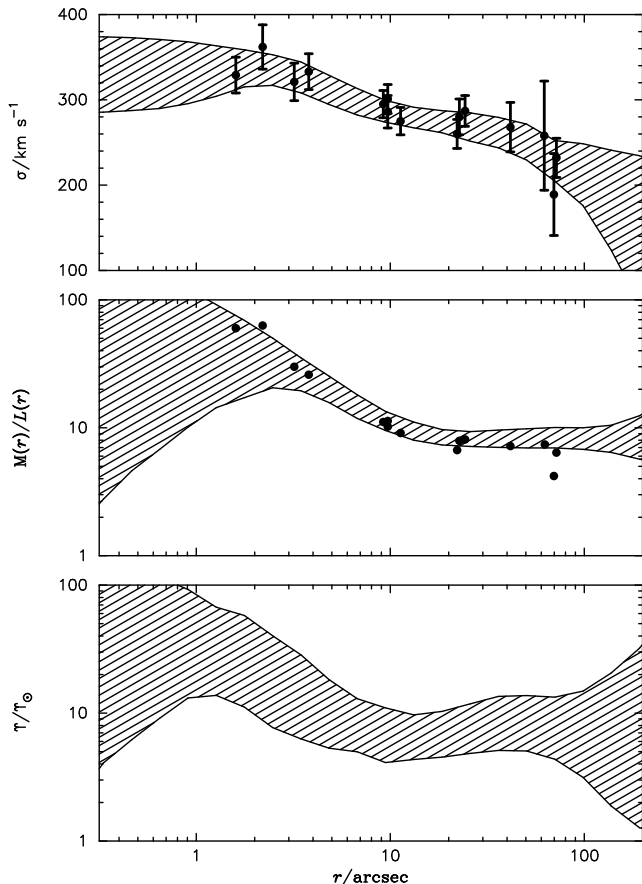


Figure 2. Our model for the mass distribution of M87, using the data of Sargent et al. (1978) and assuming the galaxy is isotropic ($\beta = 0$). The bottom panel shows the 95% confidence limits on the local mass-to-light ratio $\Upsilon(r)$. The corresponding limits on the “global” mass-to-light ratio $M(r)/L(r)$ and the model’s projected velocity dispersions are plotted on the panels above. For comparison, the points show the $M(r)/L(r)$ obtained by Sargent et al. (middle panel) and the observed dispersions (top panel).

the following ansatz for the DF (Cuddeford 1991):

$$f(\mathcal{E}, L^2) = L^{-2\beta_0} f_0(Q) \quad \text{with } Q \equiv \mathcal{E} - \frac{L^2}{2r_a^2}. \quad (16)$$

We assume that $f_0(Q) = 0$ for $Q < 0$. The luminosity density of these models

$$j(r) = 2^{3/2-\beta_0} \pi^{3/2} r^{-2\beta_0} \left(1 + \frac{r^2}{r_a^2}\right)^{-(1-\beta_0)} \frac{\Gamma(1-\beta_0)}{\Gamma(\frac{3}{2}-\beta_0)} \times \int_0^{\psi(r)} f_0(Q) (\psi - Q)^{1/2-\beta_0} dQ, \quad (17)$$

where $\psi(r)$ is related to the gravitational potential $\Phi(r)$ through $\psi(r) \equiv -\Phi(r)$. This demonstrates that the function $f_0(Q)$ is (implicitly) determined once the luminosity density $j(r)$ and mass distribution are specified.

More generally, the non-trivial velocity moments of these models are given by

$$[v_r^{2k} v_\phi^{2l} v_\theta^{2m}](r) = j \overline{v_r^{2k} v_\phi^{2l} v_\theta^{2m}}(r) = C_{klm}(r) V_{k+l+m}(r), \quad (18)$$

where

$$V_n(r) \equiv \int_0^{\psi(r)} f_0(Q) (\psi - Q)^{n-\beta_0+1/2} dQ, \quad (19)$$

and the coefficients

$$C_{klm} = 2^{k+l+m+1/2-\beta_0} r^{-2\beta_0} \left(1 + \frac{r^2}{r_a^2}\right)^{-(l+m+1-\beta_0)} \times B\left(k + \frac{1}{2}, l + m + 1 - \beta_0\right) B\left(\frac{l+1}{2}, \frac{n+1}{2}\right). \quad (20)$$

This helps to clarify the meaning of the parameters β and r_a : from (18) and (20), the anisotropy

$$\beta(r) \equiv 1 - \frac{\sigma_\phi^2}{\sigma_r^2} = \frac{r^2 + \beta_0 r_a^2}{r^2 + r_a^2}, \quad (21)$$

which tends to β_0 as $r \rightarrow 0$, and to 1 for $r \gg r_a$.

4.1 From $\Upsilon(r)$ to VPs

It is straightforward to extend the method of section 3 to calculate the higher-order moments (18) and reconstruct the VPs from them. Our method avoids the difficult problem of obtaining $f_0(Q)$ explicitly from (17). It closely follows the approach of Magorrian & Binney (1994).

Integrating (19) by parts gives

$$V_n(r) = (n - \beta_0 + 1/2) \int_r^\infty V_{n-1}(r') \frac{GM(r')}{r'^2} dr', \quad (22)$$

which is the higher-order analogue of the Jeans’ equation (3). Having V_0 from $j(r)$, it allows the full set of V_n up to any arbitrary order to be calculated. The moments $[v_r^{2k} v_\phi^{2l} v_\theta^{2m}](r)$ then follow from (18) and (20). Projecting the n^{th} -order moments along lines of sight and convolving with seeing as in Section 2 yields the classical moments of the VPs $\mathcal{L}(R; v_p)$, namely

$$[v_p^n](R) \equiv \overline{I v_p^n}(R) \equiv I(R) \int_{-\infty}^\infty \mathcal{L}(R; v_p) v_p^n dv_p. \quad (23)$$

Each VP can be reconstructed from its moments $\overline{v_p^n}$ using a Gram-Charlier series of type A (Kendall & Stuart 1943):

$$\mathcal{L}(v_p) = \frac{\alpha(w_g)}{\sigma_g} \sum_{i=0}^m d_i H_{e_i}(w_g), \quad (24)$$

where $w_g \equiv v_p/\sigma_g$, $\alpha(x) \equiv \exp(-x^2/2)/\sqrt{2\pi}$ is the standard Gaussian, the H_{e_i} are Hermite Polynomials of the first kind (e.g., Abramowitz & Stegun 1965), and the coefficients

$$d_i(\sigma_g) \equiv \int_{-\infty}^\infty \mathcal{L}(v_p) H_{e_i}(w_g) dv_p \quad (25)$$

are just linear combinations of the $\overline{v_p^n}$. Kendall & Stuart (1943) give conditions sufficient for convergence. For realistic VPs to be well-approximated using a small number of d_i , the expansion variable σ_g should be chosen so that $\sigma_g^2 \sim v_p^2$.

As in §3.1, many of the coefficients involved in the numerical evaluation of the V_n , $\overline{v_p^n}$ and d_i depend only on β_0 , r_a and $j(r)$ and therefore need only be calculated once, significantly speeding up the calculation of the $d_i(R)$ from $\Upsilon(r)$.

4.2 Comparing model and observed VPs

Since VPs are usually close to Gaussian, observed VPs are usually reported by giving the first few terms of their Gauss–Hermite expansion (van der Marel & Franx 1993; see also Gerhard 1993):

$$\mathcal{L}(v_p) = \frac{\gamma_g \alpha(w_g)}{\sigma_g} \sum_{i=0}^{\infty} h_{2i} H_{2i}(w_g), \quad (26)$$

where $w_g \equiv v_p/\sigma_g$, and the H_i are Hermite polynomials of the second kind. There is a different set of Gauss–Hermite coefficients (h_0, h_2, h_4, \dots) for each choice of (γ_g, σ_g) , but observers fix the latter to be the line-strength and dispersion of the best-fitting Gaussian to the VP. Then $h_0 = 1$, $h_2 = 0$ and the lowest-order deviation of the VP from the best-fitting Gaussian is measured by h_4 (van der Marel & Franx 1993).

While the most straightforward course of action would be to compare models and observations using this choice of (γ_g, σ_g) , this has the minor disadvantage that it can only give model predictions \hat{h}_i at the same radii as the observations. To remedy this, we instead choose $\gamma_g = 1$, and $\sigma_g(R)$ equal to the smoothly varying dispersion of the best-fit initial model (13). We use the relations (Magorrian & Binney 1994)

$$\begin{aligned} \frac{\partial h_l}{\partial \gamma_g} &= -\frac{1}{\gamma_g} h_l, \\ \frac{\partial h_l}{\partial \sigma_g} &= \frac{1}{2\sigma_g} \left(\sqrt{(l+2)(l+1)} h_{l+2} + h_l - \sqrt{l(l-1)} h_{l-2} \right), \end{aligned} \quad (27)$$

to make the small adjustments required to bring the Gauss–Hermite coefficients of the observed VPs to this choice of $(\gamma_g, \sigma_g(R))$. Conversely, when presenting our final results, we will use these relations to return the model VPs in the observational parametrization $(\gamma_g, \sigma_g, h_4, h_6, \dots)$ by adjusting (γ_g, σ_g) so that $(\hat{h}_0, \hat{h}_2) = (1, 0)$.

The Gauss–Hermite coefficients of the model galaxy, $\hat{h}_i(R)$, can be obtained from the moments $\overline{v_p^i}$ using the Gram–Charlier expansion (24) and some judicious manipulation of integrals of Hermite polynomials. Magorrian & Binney (1994) show that there is a simple linear relation between the two, namely

$$\hat{h}_k = \sum_{l=0}^{\infty} c_{kl} d_l, \quad (28)$$

and describe how to obtain the matrix $c_{kl}(\gamma_g, \sigma_g)$. Of course, in practice it is neither possible nor necessary to include all the terms in these infinite sums. Limited spectral resolution together with the effects of template mismatch mean that observations can only yield sensible information on the h_i up to $i = N_h \simeq 4$. For most of our models we find that the error in the predicted \hat{h}_4 introduced by truncating the series (28) at $l = 10$ is of order 0.002, much less than typical observational uncertainties. As a stronger test of our moment-based VP calculations, we have calculated the VPs of various models by solving eq. (17) numerically and integrating directly over the DF. The h_4 coefficients calculated this way differ from the moment-based results by less than 0.002.

To first order, errors in the h_i are uncorrelated (van der Marel & Franx 1993). Assuming that these errors are

Gaussian, the likelihood of the trial $\Upsilon(r)$ is given by

$$p(D|\Upsilon, \beta_0, r_a) = \exp\left(-\frac{1}{2}\chi_h^2\right) \quad (29)$$

with

$$\chi_h^2[\Upsilon, \beta_0, r_a] = \sum_{i=1}^N \sum_{j=0}^{N_h} \left(\frac{\hat{h}_j(R_i) - h_j(R_i)}{\Delta h_j(R_i)} \right)^2. \quad (30)$$

In practice we truncate this series at $j = 2$, since the unknown flattening of the galaxy affects its h_4 profile (i.e., we calculate the full VPs, but fit only to σ). Our method can easily be modified to deal with other parametrizations of VPs, including so-called “non-parametric” parametrizations. In most cases, however, a proper treatment of the correlations between the parameters is likely to lead to a significant increase in the complexity of the expression for the likelihood.

4.3 Including discrete tracers of the VPs

The rapid fall-off in the surface brightness of galaxies means that it is very difficult to use stellar absorption lines to measure VP shapes reliably far from the galaxy centre. Fortunately, in any galaxy there will be many stars that have evolved into planetary nebulae (PNe). These objects emit a significant fraction of their light in the O [III] line at 5007Å, making it easy to measure their line-of-sight velocities. If we make the reasonable assumption that PNe are drawn from the same DF as the stars, then the probability that a PN at projected radius R will have line-of-sight velocity between v_p and $v_p + dv_p$ is just $\mathcal{L}(R; v_p) dv_p$. Therefore the likelihood of measuring N_{PN} PNe, the i^{th} at radius R_i with line-of-sight velocity v_i and error Δv_i ,

$$p(D_{\text{PN}}|\Upsilon, \beta_0, r_a) \propto \prod_{i=1}^{N_{\text{PN}}} \mathcal{L}(R_i; v_i) \Delta v_i, \quad (31)$$

assuming that the observational uncertainties $\Delta v_i \ll \sigma(R_i)$. Then, using the results from §4.2 above, the combined likelihood of the PNe and VP data is

$$\begin{aligned} p(D|\Upsilon, \beta_0, r_a) &= p(D_{\text{VP}}|\Upsilon, \beta_0, r_a) p(D_{\text{PN}}|\Upsilon, \beta_0, r_a) \\ &\propto \exp\left(-\frac{1}{2}\chi_h^2\right) \prod_{i=1}^{N_{\text{PN}}} \mathcal{L}(R_i, v_i) \Delta v_i. \end{aligned} \quad (32)$$

Since the shape of $\mathcal{L}(R, v)$ is affected by the galaxy’s unknown flattening, in practice we simply ignore the deviations of the model’s predicted $\mathcal{L}(R, v)$ from their best-fit Gaussians, consistent with our treatment of h_4 measurements above.

4.4 Summary

In summary then, the procedure we use to obtain the range of $\Upsilon(r)$ consistent with observed VPs is as follows:

- (1) Fit an initial guess of the form (13) to the observed dispersions σ_i .
- (2) Use (27) to adjust the observed Gauss–Hermite coefficients h_i to $\gamma_g = 1$ and $\sigma_g(R)$ equal to the dispersion profile of this smooth initial fit.
- (3) Iterate the Metropolis algorithm as in §3.2, but including higher-order (typically up to 10th-order) moments

(§4.1) rather than just the second-order moments (§3.1). Use the likelihood (32) instead of (10).

- (4) When the Metropolis algorithm is finished, calculate the confidence limits on the model $\Upsilon(r)$, and the corresponding \hat{h}_i . Convert the latter back to the observational parametrization $(\gamma_g, \sigma_g, h_4, \dots)$ using (27).

If we somehow knew that the galaxy was close to spherical, we could constrain its anisotropy by constructing models with a variety of β_0 and r_a and using equation (14) to find the range of (β_0, r_a) preferred by the available data. In practice, however, we construct models for just a few choices of (β_0, r_a) , compare the predicted σ and h_4 profiles with the observations and use the results of Appendix A to estimate the allowed range of flattening or anisotropy in the real galaxy.

5 APPLICATION TO REAL GALAXIES

In this section we apply the machinery to a number of real galaxies, listed in Table 1. The sample consists of galaxies no flatter than E2 on the sky, with published kinematics measured out to of order the galaxy’s effective radius or further. For most of the galaxies the available data consist simply of a velocity dispersion profile, but in a handful of cases measurements of the shapes of the VPs (h_4 parameters) are also available. Two of the galaxies have PNe radial-velocity measurements: 15 radial velocities for M32, 29 for NGC 3379.

We obtain the luminosity density $j(r)$ of each galaxy by deprojecting its spherically averaged surface brightness distribution using the method described in Magorrian (1999) with $n_r = 30$ radial grid points. Then we apply the machinery of §4 using the observed kinematics to constrain the galaxy’s mass profile, first under the assumption that the galaxy is isotropic ($\beta = 0$), then assuming that it is mildly radially anisotropic ($\beta = 0.3$). In each case we carry out 10^5 iterations of the Metropolis algorithm, including terms up to $l = 10$ in equation (24). But, given the degeneracy between anisotropy and flattening identified above, we ignore any measurements of VP shapes, and fit simply to the velocity dispersion profile (i.e., we truncate the series (30) at $N_h = 2$), and merely predict the h_4 profile for a spherical galaxy with the assumed anisotropy.

5.1 Results for individual galaxies

The results of this modelling are plotted on Figure 3. One of the most obvious features of the results is that each model’s outer mass profile is almost independent of the anisotropy we assume (Efstathiou, Ellis & Carter 1980; Gerhard 1993). Some of the galaxies deserve more detailed comment.

M32 Our models use the minor-axis velocity dispersion profile obtained by van der Marel et al. (1994) and the 15 PNe radial velocities measured by Nolthenius & Ford (1986). These data are insufficient to place any interesting constraints on whether M32 has a halo or not: the $v_c(r)$ and $\Upsilon(r)$ profiles of our models are both consistent with being flat. The results plotted are for models where we have subtracted a heliocentric systemic velocity of -203 km s^{-1} (Tully 1988) from the PNe velocities. Assuming systemic velocities of -195 km s^{-1} or -185 km s^{-1} (Nolthenius & Ford 1986) yields almost identical results.

NGC 2434 As mentioned in §2, Rix et al. (1997) have used Schwarzschild’s method to construct spherical models of this galaxy. Their models required a dark halo with

$v_c \simeq 300 \text{ km s}^{-1}$ at around r_{eff} . Our results are in very good agreement. We re-iterate, however, that if this galaxy were flattened along the line of sight these spherical models would underestimate the true circular velocity.

NGC 3379 Our models use the minor-axis dispersion profile measured by Statler & Smecker-Hane (1999), and the 29 PNe radial velocities from Ciardullo, Jacoby & Dejonghe (1993). We have subtracted a systemic velocity of 900 km s^{-1} from the PNe velocities for the model plotted in Fig. 3. The results are almost identical if we instead assume a systemic velocity of 916 km s^{-1} , equal to the mean recession velocity of the PNe sample, or if we use the 881 km s^{-1} quoted in Tully (1988). Statler & Smecker-Hane (1999) discovered that this galaxy has a kink in its dispersion profile at a radius of ~ 15 arcsec. Our models fit the data beyond the kink by having $\Upsilon(r)$ increase by a factor of three between 15 arcsec and 60 arcsec, then becoming further out in order to fit the PNe radial velocities. An alternative explanation is that NGC 3379 may be a face-on S0 (e.g., Capaccioli et al. 1991), or a weakly triaxial system viewed face on (Statler & Smecker-Hane 1999). We note that the the evidence for positive h_4 in this galaxy could be due either to radial anisotropy (Gebhardt et al. 2000) or to the galaxy being flattened system viewed face on (Section 2).

NGC 4472 Brighenti & Mathews’ (1997) modelling of the X-ray emission from this galaxy indicates a mass of about $3 \times 10^{11} M_\odot$ within 7.8 kpc (scaling to our assumed distance of 15.3 Mpc), which corresponds to $v_c \simeq 410 \text{ km s}^{-1}$. Similar results are found by Irwin & Sarazin (1996). This is in good agreement with our $v_c = (419 \pm 11) \text{ km s}^{-1}$ at $1r_{\text{eff}} = 7.8 \text{ kpc}$.

NGC 4486 Nulsen & Böhringer (1995) find that the X-ray data for M87 are consistent with a mass per unit length of $3.6 \times 10^{10} M_\odot \text{ kpc}^{-1}$, or $v_c = 390 \text{ km s}^{-1}$. Similarly, Tsai (1993) finds a mass $2.8 \times 10^{11} M_\odot$ enclosed within a radius 7.8 kpc, also giving $v_c = 390 \text{ km s}^{-1}$. Using the velocity dispersion measurements of Sembach & Tonry (1996), our models find $v_c = (530 \pm 9) \text{ km s}^{-1}$, larger by 30%. Part of this discrepancy is due to the fact that Sembach & Tonry’s measurements are systematically offset by 10 to 15% (Sembach, private communication). Comparison with the measurements of Sargent et al. (1978), Bender, Saglia & Gerhard (1994) and van der Marel (1994) confirms that Sembach & Tonry’s measurements are systematically overestimated by about 15%.

Taking our models at face value, five of the galaxies in the sample (M87, NGC 2434, 4472, 5846 and 7796) show evidence for a dark halo (flat rotation curve and rising mass-to-light ratio at large radii). Five (NGC 1379, 4434, 4552, 7192, 7507) show evidence against a dark halo (constant mass-to-light ratio and falling rotation curve). It should be borne in mind, however, that these results depend critically on our assumption of spherical symmetry. For example, in our model of NGC 4552 the rotation curve falls off at large radii, and mass follows light very closely. Despite being round on the sky, however, this galaxy is classified as an S0 in some catalogues. If its light distribution did indeed become significantly flattened at large radii, then it would have to have a rising mass-to-light ratio profile, and possibly a flat rotation curve.

The remaining eight galaxies (M32, NGC 1400, 3379,

Table 1. Sources of data used.

Name	Dist. (Mpc)	B_T	$\log L_B$ (L_\odot)	$B - V$	$V - I$	r_{eff} (arcsec)	Phot. Source	Kin. Source	r_{max} (arcsec)	$v_c(r_{\text{eff}})$ (km s^{-1})
(1)	(2)	(3)	(4)	(5)	(6)	(7)	(8)	(9)	(10)	(11)
M32	0.8	8.76	8.49	0.89	1.14	40	K87	vdM94	22	75 ± 15
								NF86 (PNe)	271	
NGC 1379	17.9	11.66	10.03	0.91	1.19	24	FIH89	GCBZL98	61	167 ± 5
NGC 1400	21.5	11.62	10.21	1.03	1.37	38	L85	BBDDSSZZ94	45	268 ± 20
NGC 2434	20.0	11.43	10.22	0.91	1.18	24	CD94	CZMDQ95	62	296 ± 17
NGC 3379	9.9	10.43	10.01	0.99	1.23	35	PDIDC90	SS99	78	262 ± 14
								CJD93 (PNe)	209	
NGC 4434	15.3	12.83	9.43	–	–	19	CCR90	SP97	17	142 ± 18
NGC 4464	15.3	13.61	9.12	0.89	1.19	6	CCR90	SF97	17	165 ± 13
NGC 4467	15.3	14.81	8.64	–	–	10	–	BN90	9	98 ± 10
NGC 4472	15.3	9.32	10.83	0.99	1.26	105	PDIDC90	FIF95*	140	419 ± 23
NGC 4478	15.3	12.14	9.71	0.90	1.19	14	CCR90	DEFIS83	27	220 ± 13
M87	15.3	9.52	10.75	0.98	1.27	105	PDIDC90	ST96	170	531 ± 17
NGC 4494	15.3	10.69	10.29	–	–	45	BM87	JS89*	37	240 ± 25
NGC 4552	15.3	10.84	10.23	0.97	1.20	30	MM94	SP97	58	330 ± 17
NGC 5846	26.0	10.67	10.75	–	–	63	MM94	ST96	145	418 ± 20
NGC 6407	60.0	12.90	10.59	1.12	1.38	33	CD94	CD94*	43	440 ± 32
NGC 7192	34.0	12.04	10.44	0.97	1.24	28	CD94	CD94*	43	308 ± 23
NGC 7507	21.0	11.15	10.38	1.00	1.28	31	FIH89	BBDDSSZZ94	66	321 ± 16
NGC 7796	37.0	12.28	10.42	1.00	1.23	37	SWJTB91	BBDDSSZZ94	37	371 ± 30

Distances (col. 2) are taken (in decreasing order of preference) from Faber et al. (1997), Faber et al. (1989) or the Hubble relation assuming $H_0 = 80 \text{ km s}^{-1} \text{ Mpc}^{-1}$. B magnitudes, $B - V$ colours and effective radii (cols. 3, 5 and 7) are taken from Faber et al. (1989). $V - I$ colours (col. 6) are from Prugniel et al. (1993) and Poulain & Nieto (1994). The photometry used (col. 8) is supplemented with HST photometry from Faber et al. (1997) when available. Col. 10 gives the radius of the outermost observed point of the kinematic source (col. 9). Our models use velocity dispersions along one axis (usually the minor if available), except for sources marked with an asterisk for which we use results from multiple slit positions. Col. (11) gives the 95% confidence intervals on the circular velocities of the isotropic models at one effective radius.

4464, 4467, 4478, 4494 and 6407) are indeterminate, with both a flat mass-to-light ratio and a flat rotation curve at the outermost available radius. The most sensible way of distinguishing between constant- Υ and constant- v_c models of these galaxies would be by using PNe to estimate the galaxy’s mean luminosity-weighted velocity dispersion outside the radius of the outermost stellar velocity dispersion. In Appendix B we show that distinguishing between constant- Υ and constant- v_c models with 95% confidence would require radial velocities of ~ 100 such PNe.

5.2 The Tully–Fisher relation for ellipticals

Figure 4 plots the circular velocity derived by our models at $1r_{\text{eff}}$ versus galaxy luminosity. They lie on a Tully–Fisher relation parallel to that for spiral galaxies, as was first noted by Franx (1993). Our elliptical Tully–Fisher relation is offset from Pierce & Tully’s (1992) spiral relation in the sense that, for given v_c , ellipticals are fainter than spirals by 1.5 mag (B band) or 1.0 mag (I band). The offset from Mathewson, Ford & Buchhorn’s (1992) sample is 0.83 mag in I . Of course, these numbers are underestimates (overestimates) of the true offset if our ellipticals are oblate (prolate) galaxies viewed face on.

The scatter in our Tully–Fisher relation for ellipticals is 0.55 mag, significantly larger than the values ~ 0.2 mag reported for samples of nearby spirals. But the scatter in the real $v_c - L$ correlation for ellipticals could well be smaller than 0.55 mag: our galaxy sample is heterogenous, precluding accurate distance (and therefore luminosity) estimates,

and we are unable to correct our circular velocities for the unknown flattening of our galaxies, a problem that is usually unavoidable when using elliptical galaxies.

Our results differ from those of Neistein et al. (1999), who looked for a Tully–Fisher relation in a sample of nearby S0 galaxies, using the method of surface brightness fluctuations to obtain careful distance estimates, and obtaining circular velocities by deprojecting the galaxies’ observed stellar kinematics. They found a relation with an intrinsic scatter of 0.7 mag (I band), with S0s of given v_c only 0.5 mag fainter than corresponding type-Sc spirals. This is less than expected if S0s are former spirals with truncated star formation histories. Our results can only be brought into broad agreement with theirs if we assume that our round ellipticals are mostly face-on prolate systems. Their method, however, also requires assumptions about the intrinsic shapes of their galaxies, although it is unclear whether this could explain the worryingly small 0.5 mag offset between S0s and spirals.

6 CONCLUSIONS

We have determined the outer mass profiles in a sample of 18 round galaxies, under the assumption that each is spherical and has constant anisotropy. The assumption of spherical symmetry is the more dangerous of the two: if a galaxy is flattened along the line of sight, our spherical models underestimate its mass, whereas varying the anisotropy has little effect on the outer mass profile. Nevertheless, if we assume that a galaxy’s anisotropy and the flattening of its light distribution and of its equipotential surfaces do not vary

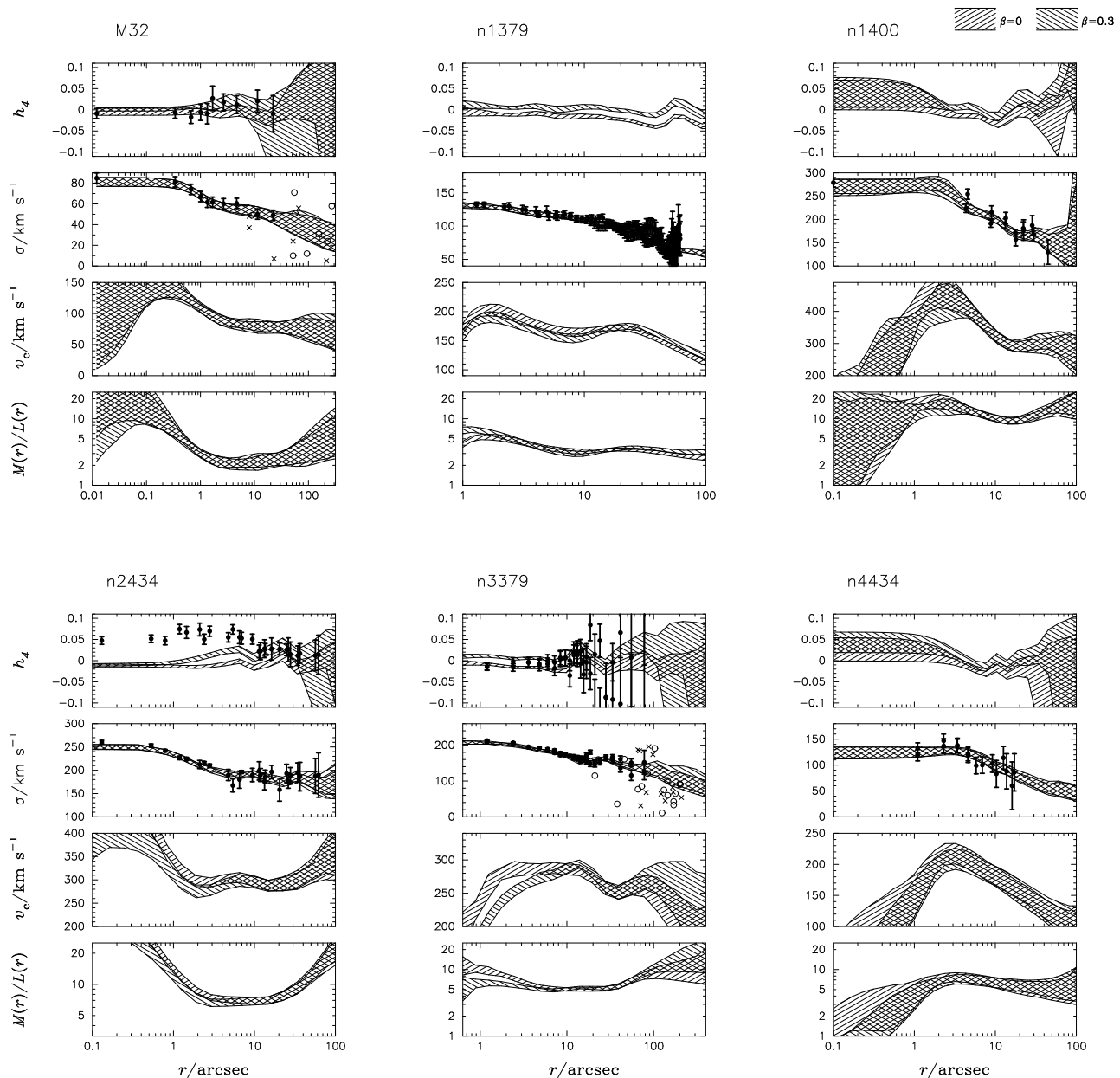


Figure 3. Model fits for mass-to-light ratios, circular velocities and projected kinematics for the galaxies in our sample. The hatched regions give the 95% confidence bands for each quantity. For each galaxy an isotropic ($\beta = 0$) and a mildly radially anisotropic ($\beta = 0.3$) model is constructed by varying the local mass-to-light ratio to fit the observed dispersion profile. The h_4 profiles plotted are model predictions, not fits. The PNe measurements used in our models of M32 and NGC 3379 are plotted as the crosses ($v < 0$) and open circles ($v > 0$).

strongly with radius then we may sensibly use our spherical models to check for evidence of a dark halo (i.e., a rise in mass-to-light ratio with radius).

Our results are somewhat unsurprising. There is very clear evidence for massive dark haloes in large ellipticals, whereas the case for smaller galaxies is more ambiguous. Our early-type galaxies follow a Tully–Fisher relation parallel to that for spiral galaxies, but offset by at least 0.8 mag (I -band). This is larger than the offset found by Neistein et al. (1999) for their sample of S0 galaxies, but is reassuringly consistent with what one would expect from passive stellar evolution.

The degeneracy between anisotropy and shape pointed out in §2 (see also Magorrian 1999) means that we are unable to place strong constraints on the anisotropies of our galaxies. It is often claimed that elliptical galaxies are radially anisotropic, but there is surprisingly little solid evidence for this assertion. For example, detailed dynamical models have been constructed for the intermediate-luminosity ellipticals NGC 2434 (Rix et al. 1997), NGC 3379 (Gebhardt et al. 2000) and NGC 6703 (Gerhard et al. 1998). In all cases, the models were required to become radially anisotropic in order to fit the observed VP shapes, but in all cases it was unjustifiably assumed that the galaxy was either spherical

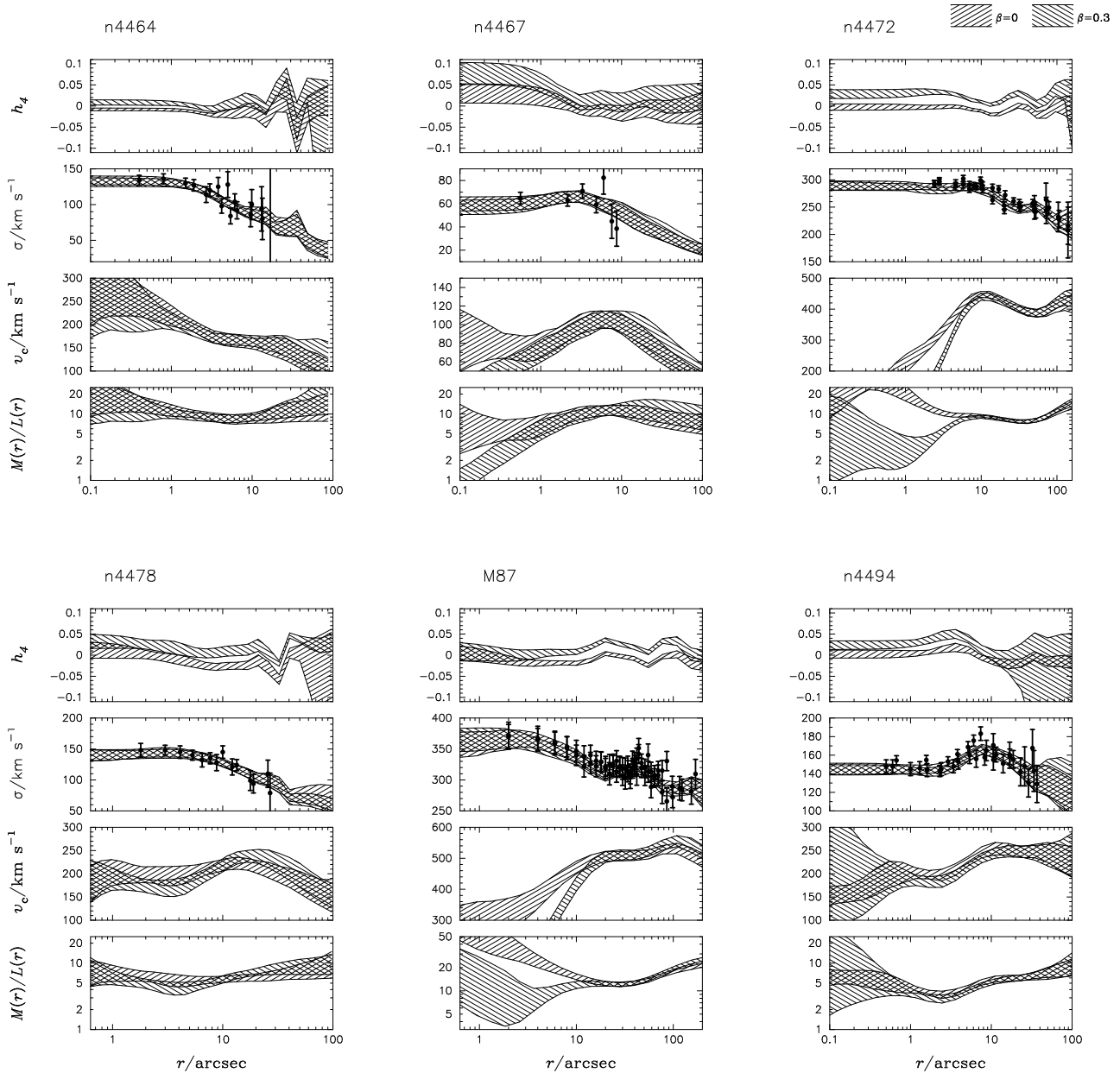


Figure 3. continued...

or spheroidal – isotropic models with weak face-on disks can also provide reasonable fits to the VPs of these galaxies.

Brighter ellipticals suffer less from this degeneracy, since they are unlikely to be disk. The strongest evidence for radial anisotropy in an elliptical galaxy comes from Matthias & Gerhard’s (1999) investigation of NGC 1600, a boxy E4 galaxy. Their best-fit model has an anisotropy $\beta \simeq 0.5$ in the equatorial plane and $\beta \simeq 0$ along the symmetry axis. Since this galaxy is so strongly flattened in projection, it must be close to edge on, minimizing the uncertainties in the shape of its intrinsic light distribution, and, therefore, its mass profile and anisotropy (provided one makes the reasonable assumption that its mass distribution is not significantly flatter than its light distribution).

It is unlikely that one will ever be able to directly place strong constraints on the intrinsic shapes (and therefore

anisotropies and masses) of round galaxies. To gain a proper understanding of the dynamical nature of elliptical galaxies, it would be more sensible to start with a thorough investigation of the shapes and profiles of the dark and luminous matter in flattened systems like NGC 1600. Models of these galaxies when “observed” face-on could then prove to be an interesting test of the nature of rounder galaxies.

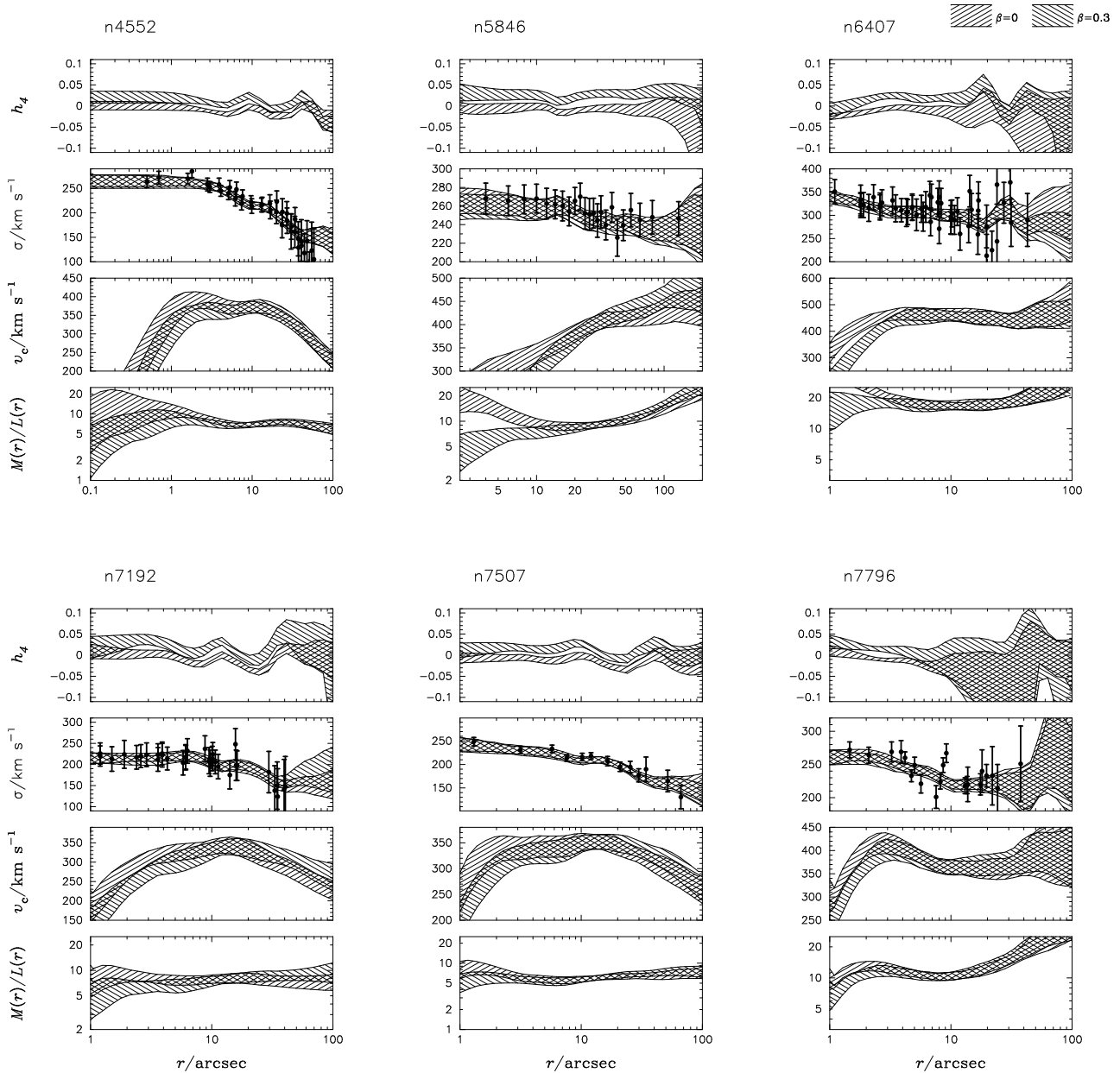


Figure 3. continued.

ACKNOWLEDGMENTS

We thank Scott Tremaine for helpful advice, Marijn Franx and John Hibbard for useful discussions, and Ortwin Gerhard for comments on a draft of the manuscript. Financial support was provided by NSERC and PPARC. D.R.B. participated originally via the Physics Co-op program of the University of Victoria, Canada.

REFERENCES

- Abramowitz M., Stegun I.A., 1965, Handbook of Mathematical Functions. Dover, New York
- Bender R., Möllenhoff C., 1987, *A&A*, 177, 71 (BM87)
- Bender R., Nieto J.-L., 1990, *A&A*, 239, 97 (BN90)
- Bender R., Saglia R.P., Gerhard O., 1994, *MNRAS*, 269, 785
- Bertin G., Bertola F., Buson L.M., Danziger I.J., Dejonghe H., Sadler E.M., Saglia R.P., de Zeeuw P.T., Zeilinger W.W., 1994, *A&A*, 292, 381 (BBDDSSZZ94)
- Binney J., 1978, *MNRAS*, 183, 501
- Binney J., Tremaine S., 1987, *Galactic Dynamics* (Princeton: Princeton University Press)
- Brighenti F., Mathews W.G., 1997, *ApJ*, 486, L83
- Buote D.A., Canizares C.R., 1997, *ApJ*, 474, 650
- Capaccioli M., Vietri M., Held E.V., Lorenz H., 1991, *ApJ*, 371, 535
- Caon N., Capaccioli M., Rampazzo R., 1990, *A&AS*, 86, 429 (CCR90)
- Carollo C.M., Danziger I.J., 1994, *MNRAS*, 270, 523 (CD94)
- Carollo C.M., de Zeeuw P.T., van der Marel R.P., Danziger I.J., Qian E.E., 1995, *ApJ*, 441, 25 (CZMDQ95)
- Ciardullo R., Jacoby G.H., Dejonghe H.B., 1993, *ApJ*, 414, 454 (CJD93)

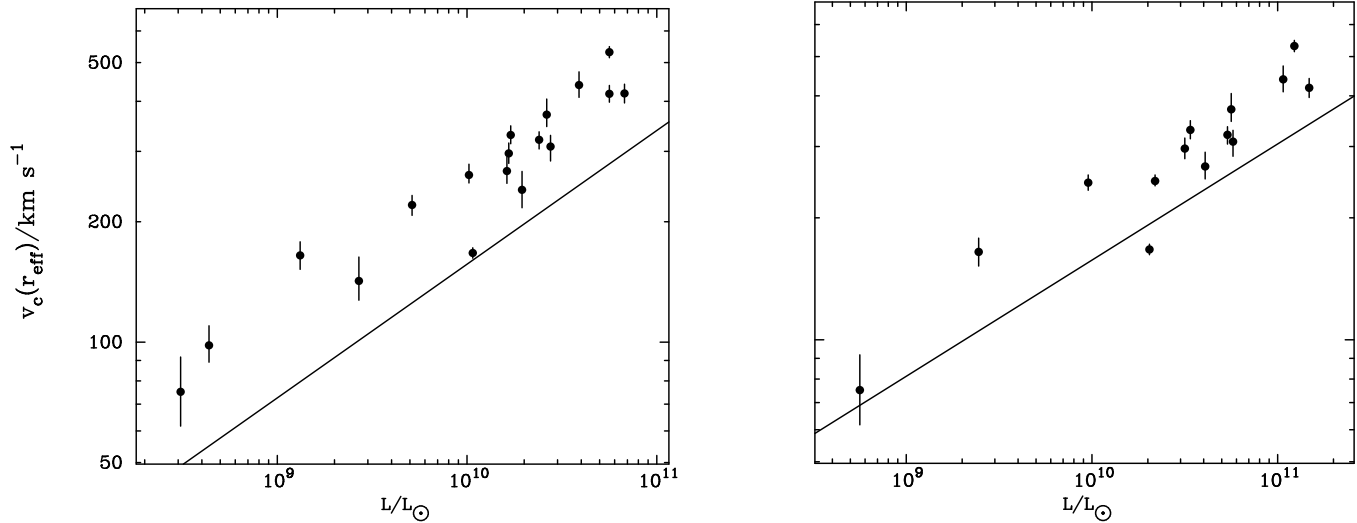


Figure 4. Tully–Fisher relation for our sample of early-type galaxies. The points plot the 95% confidence bounds on the circular velocity at $1r_{\text{eff}}$ against B -band (left panel) and I -band (right panel) luminosities. For comparison, the straight lines plot the Tully–Fisher relation for spirals as found by Pierce & Tully (1992).

Cuddeford P., 1991, *MNRAS*, 253, 414
 Davies R.L., Efstathiou G., Fall S.M., Illingworth G., Schechter P.L., 1983, *ApJ*, 266, 41 (DEFIS83)
 Efstathiou G., Ellis R.S., Carter D., 1980, *MNRAS*, 193, 931
 Faber S.M., Wegner G., Burstein D., Davies R.L., Dressler A., Lynden-Bell D., Terlevich R.J., 1989, *ApJS*, 69, 763
 Faber S.M., et al., 1997, *AJ*, 114, 1771
 Fisher D., Illingworth G., Franx M., 1995, *ApJ*, 438, 539 (FIF95)
 Franx M., 1993, in Dejonghe H., Habing H.J., eds., *Proc. IAU Symp. 153, Galactic Bulges*. Kluwer, Dordrecht, p.243
 Franx M., Illingworth G., Heckman T., 1989, *AJ*, 98, 538 (FIH89)
 Gebhardt K., Fischer P., 1995, *AJ*, 109, 209
 Gebhardt K., et al., 2000, *AJ*, 119, 1157
 Gerhard O.E., 1993, *MNRAS*, 265, 213
 Gerhard O.E., Jeske G., Saglia R.P., Bender R., 1998, *MNRAS*, 295, 197
 Graham A.W., Colless M.M., Busarello G., Zaggia S., Longo G., 1998, *A&AS*, 133, 325 (GCBZL98)
 Irwin J.A., Sarazin C.L., 1996, *ApJ*, 471, 683
 Jedrzejewski R., Schechter P.L., 1989, *AJ*, 98, 147 (JS89)
 Kendall M.G., Stuart A., 1943, *The Advanced Theory of Statistics*. Charles Griffin & Co., London
 Kent S.M., 1987, *AJ*, 94, 306 (K87)
 Kochanek C.S., 1996, *ApJ*, 466, 638
 Lauer T.R., 1985, *ApJS*, 57, 473 (L85)
 Loewenstein M., White R.E., 1999, *ApJ*, 518, 50
 Magorrian S.J., Binney J., 1994, *MNRAS*, 271, 949
 Magorrian S.J., 1999, *MNRAS*, 302, 530
 Matthias M., Gerhard O.E., 1999, *MNRAS*, 310, 879
 Mathewson D.S., Ford V.L., Buchhorn M., 1992, *ApJS*, 81, 413
 Merritt D., 1993, *ApJ*, 413, 79
 Merritt D., 1996, *AJ*, 112, 1085
 Merritt D., Saha P., 1993, *ApJ*, 409, 75
 Merritt D., Tremblay B., 1993, *AJ*, 106, 2229
 Metropolis N., Rosenbluth A., Rosenbluth M., Teller A., Teller E., 1953, *J. Chem. Phys.*, 21, 1087
 Michard R., Marchal J., 1994, *A&AS*, 105, 481 (MM94)
 Neistein E., Maoz D., Rix H.-W., Tonry J.L., 1999, *AJ*, 117, 2666
 Nulsen P.E.J., Böhringer H., 1995, *MNRAS*, 274, 1093
 Nolthenius R., Ford H., 1986, *ApJ*, 305, 600 (NF86)

Peletier R.F., Davies R.L., Illingworth G.D., Davis L.E., Cawson M., 1990, *AJ*, 100, 1091 (PDIDC90)
 Pierce M.J., Tully R.B., 1992, *ApJ*, 387, 47
 Press W.H., Flannery B.P., Teukolsky S.A., Vetterling W.T., 1992, *Numerical Recipes in C*, 2nd edn. Cambridge Univ. Press, Cambridge
 Prugniel P., Bica E., Klotz A., Alloin D., 1993, *A&AS*, 98, 229
 Poulain P., Nieto J.-L., 1994, *A&AS*, 103, 573
 Rix H.-W., de Zeeuw P.T., Cretton N., van der Marel R.P., Carollo C.M., 1997, *ApJ*, 488, 720
 Saglia R.P., Kronawitter A., Gerhard O., Bender R., *AJ*, 119, 153
 Sargent W.L.W., Young P.J., Lynds C.R., Boksenberg A., Shortridge K., Hartwick F.D.A., 1978, *ApJ*, 221, 731
 Schwarzschild M., 1979, *ApJ*, 232, 236
 Sembach K.R., Tonry J.L., 1996, *AJ*, 112, 797 (ST96)
 Simien F., Prugniel Ph., 1997, *A&AS*, 126, 15S (SP97)
 Sparks W.B., Wall J.V., Jordan P.R., Thorne D.J., van Breda I., 1991, *ApJS*, 76, 471 (SWJTB91)
 Statler T.S., Smecker-Hane T., 1999, *AJ*, 117, 839 (SS99)
 Tsai J.C., 1993, *ApJ*, 413, L59
 Tully R.B., 1988, *Nearby Galaxies Catalog*, Cambridge University Press, Cambridge
 van der Marel R.P., Franx M., 1993, *ApJ*, 407, 525
 van der Marel R.P., Rix H.-W., Carter D., Franx M., White S.D.M., de Zeeuw T., 1994, *MNRAS*, 268, 521 (vdM94)
 van der Marel R.P., 1994, *MNRAS*, 270, 271

APPENDIX A: THE DEGENERACY BETWEEN MASS, ANISOTROPY AND FLATTENING IN SCALE-FREE OBLATE GALAXY MODELS

Gerhard (1993) has carried out an extensive investigation into how anisotropy affects the VPs of simple spherical galaxy models. Here we use scale-free models to compare the effects of anisotropy with the effects of flattening the galaxy’s light distribution. For simplicity we confine our attention to spheroidal models, and ignore the effects of diskiness, boxiness or a radially varying axis ratio.

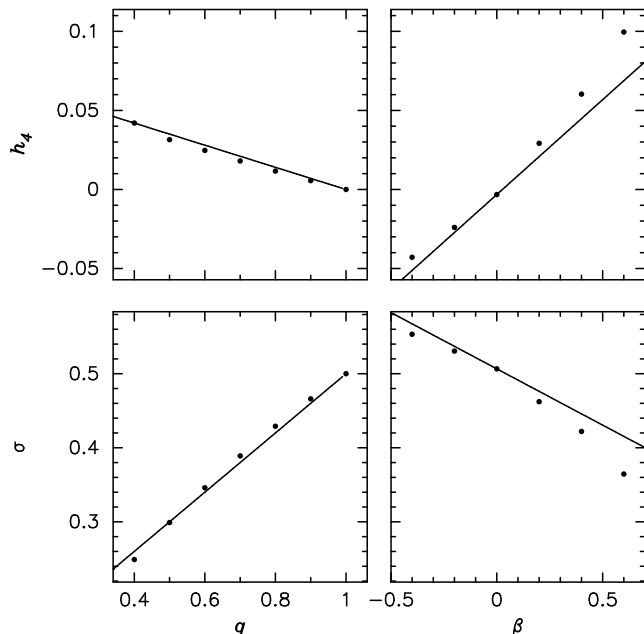


Figure 5. Degeneracy between mass, anisotropy and flattening in scale-free models. The panels on the left show how the Gauss–Hermite coefficients of the VPs of face-on oblate isotropic models vary with axis ratio. The panels on the right show how the VPs of spherical models depend on anisotropy. All models have a luminosity density profile $j \sim r^{-4}$ embedded in a spherical isothermal halo, but similar results are found for other density profiles and for a Keplerian potential. The lines plot the crude fits described in the text.

Our models have power-law density profiles

$$\nu(R, z) \propto \left(R^2 + \frac{z^2}{q^2} \right)^{-\alpha/2}, \quad (\text{A1})$$

with axis ratio q , and either Kepler $\Phi(r) = -GM/r$ or logarithmic $\Phi(r) = \frac{1}{2}v_c^2 \ln r$ potentials. We construct two orthogonal classes of models: spherical, anisotropic ($q = 1$, $\beta \neq 0$) and flattened, isotropic ($q \neq 1$, $\beta = 0$), viewed face-on.

We calculate the VPs of the flattened, isotropic models using the method described in Magorrian & Binney (1994). For the spherical anisotropic models we solve equation (16) for $f_0(Q)$ and calculate the VPs by direct integration. This gives results that are in very good agreement with the moment-based method of §4. Figure 5 shows the Gauss–Hermite coefficients of the VPs of models with $\alpha = 4$ in spherical isothermal halos with $v_c = 1$. Changing the axis ratio of one of the isotropic models by an amount Δq , the Gauss–Hermite coefficients of its VPs change by

$$\begin{aligned} \frac{\Delta\sigma}{\sigma} &\simeq 0.8\Delta q \\ \Delta h_4 &\simeq -0.07\Delta q. \end{aligned} \quad (\text{A2})$$

On the other hand, on increasing a spherical galaxy’s anisotropy by an amount $\Delta\beta$, its VPs change by

$$\begin{aligned} \frac{\Delta\sigma}{\sigma} &\simeq -0.3\Delta\beta \\ \Delta h_4 &\simeq 0.12\Delta\beta. \end{aligned} \quad (\text{A3})$$

We have checked that these expressions hold for models with $2 \lesssim \alpha \leq 4$ in both Kepler and halo potentials. The effects of

even stronger radial anisotropy can be mimicked by making the flattened galaxy slightly disk – the expressions in (A2) apply only for perfectly oblate galaxies.

There are many galaxies whose observed VPs are more centrally peaked (larger h_4) than the predictions from simple spherical isotropic models. One way of fitting these kinematics is to construct spherical or spheroidal models with mild radial anisotropy (e.g., Rix et al. 1997; Gerhard et al. 1998; Gebhardt et al. 2000; Saglia et al. 2000). An alternative is to construct flattened models that are closer to isotropic, possibly with weak, face-on stellar disks. It is reasonable to invoke such disks to explain the kinematics of intermediate-luminosity ellipticals such as NGC 2434, NGC 3379 and NGC 6703, since many galaxies of similar luminosity are observed to be isotropic and disk-like when viewed edge on. A giant elliptical like NGC 1399, however, is much less likely to have a stellar disk, meaning that the degeneracy between anisotropy and shape is more strongly constrained to lie within the limits set by (A2) and (A3).

APPENDIX B: DISTINGUISHING BETWEEN MODELS WITH DARK HALOS AND MODELS WITH CONSTANT MASS-TO-LIGHT RATIOS

Galaxies become very faint at large radii, meaning that absorption-line spectroscopy can be used to measure stellar velocity dispersions only out to some maximum radius $r_1 \sim r_{\text{eff}}$. One way of probing a galaxy’s mass distribution at radii larger than r_1 is to obtain radial velocities of a large number of PNe. Our aim in this appendix is to calculate the number of PNe that would be required to distinguish between constant- Υ and constant- v_c models at given confidence level. We assume that the anisotropy and intrinsic shape of each galaxy do not vary strongly with radius (§2).

Let us write $\hat{\sigma}_1$ for the galaxy’s projected velocity dispersion at r_1 and $\hat{\sigma}_2$ for the projected luminosity-weighted velocity dispersion averaged over radii $r > r_1$. The former is estimated by absorption-line spectroscopy, the latter from the PNe radial velocities. For $r_1 \sim r_{\text{eff}}$, we find that constant- Υ models of our galaxies predict a ratio $\hat{\mathcal{R}} \equiv \hat{\sigma}_2/\hat{\sigma}_1 \simeq 0.7$, whereas constant- v_c models of course predict $\hat{\mathcal{R}} = 1$. We write M_Υ for the model with constant mass-to-light ratio ($\hat{\mathcal{R}} \simeq 0.7$) and M_{halo} for the model with a halo ($\hat{\mathcal{R}} = 1$).

The available data D consist of an estimate $\sigma_1 \pm \Delta\sigma_1$ of $\hat{\sigma}_1$, and radial velocity measurements $v_1 \dots v_N$ of the N PNe with radii $r > r_1$. We assume that $p(\hat{\sigma}_1|D)$ is Gaussian with mean σ_1 and dispersion $\Delta\sigma_1$. The radial velocity measurements provide an estimate $\sigma_2^2 \equiv \sum v_i^2/N - (\Delta v)^2$ of $\hat{\sigma}_2^2$, where Δv is a typical error in the measured v_i . By the central limit theorem, when N is large $p(\hat{\sigma}_2|D)$ may be approximated by a Gaussian with mean σ_2 and dispersion $\Delta\sigma_2 \equiv \sigma_2[(1 + (\Delta v/\sigma_2)^2)/2N]^{1/2}$. Therefore

$$\begin{aligned} p(\sigma_1\sigma_2|\hat{\sigma}_1\hat{\sigma}_2) d\sigma_1 d\sigma_2 &= \frac{1}{2\pi} \frac{d\sigma_1 d\sigma_2}{\Delta\sigma_1 \Delta\sigma_2} \\ &\times \exp \left[-\frac{1}{2} \left(\frac{\sigma_1 - \hat{\sigma}_1}{\Delta\sigma_1} \right)^2 - \frac{1}{2} \left(\frac{\sigma_2 - \hat{\sigma}_2}{\Delta\sigma_2} \right)^2 \right]. \end{aligned} \quad (\text{B1})$$

Setting $\hat{\sigma}_2 = \hat{\mathcal{R}}\hat{\sigma}_1$, $\sigma_2 = \mathcal{R}\sigma_1$ and integrating over σ_1 yields

$$p(\mathcal{R}|\hat{\mathcal{R}})d\mathcal{R} \simeq \frac{1}{\sqrt{2\pi}} \frac{d\mathcal{R}}{\mathcal{R}(f_1^2 + f_2^2)^{1/2}} \exp\left[-\frac{1}{2} \frac{(\mathcal{R} - \hat{\mathcal{R}})^2}{\mathcal{R}^2(f_1^2 + f_2^2)}\right], \quad (\text{B2})$$

where $f_i \equiv \Delta\sigma_i/\sigma_i$ are the fractional errors on the estimates of $\hat{\sigma}_1$ and $\hat{\sigma}_2$.

For an observed dispersion ratio \mathcal{R} , Bayes' theorem gives the relative odds of M_{halo} over M_{Υ} as

$$\frac{p(M_{\text{halo}}|\mathcal{R})}{p(M_{\Upsilon}|\mathcal{R})} = \frac{p(\mathcal{R}|M_{\text{halo}}) p(M_{\text{halo}})}{p(\mathcal{R}|M_{\Upsilon}) p(M_{\Upsilon})}. \quad (\text{B3})$$

Having no prior preference for either model, we take $p(M_{\text{halo}}) = p(M_{\Upsilon})$. Now suppose that M_{Υ} were the correct model. Then the fraction of observations that will correctly choose this model over M_{halo} can be obtained by integrating $p(\mathcal{R}|M_{\Upsilon})$ over all \mathcal{R} for which the odds (B3) favour M_{Υ} . Performing this integral, we find that one must have $(f_1^2 + f_2^2)^{1/2} \lesssim 0.1$ if this fraction is to be larger than 95%. Therefore, distinguishing between constant- Υ and constant- v_c models at the 95% confidence level requires first that one have an estimate of the velocity dispersion at $r_1 \sim r_{\text{eff}}$ with fractional error $f_1 < 10\%$. If this dispersion could be measured with 5% accuracy, then one would need to measure the mean dispersion outside r_1 with a fractional error $f_2 < 8.7\%$, which could be accomplished using $N \sim 70$ PNe radial velocities.

This paper has been produced using the Royal Astronomical Society/Blackwell Science \TeX macros.